Workshop on Recent Advances in Computational Structural
Dynamics and High Performance Computing
USAE Waterways Experiment Station
April 24-26 1996

CONCRETE MATERIAL MODELING IN EXPLICIT COMPUTATIONS

L. Javier Malvar[1] and Don Simons[2]
[1] Karagozian & Case, 620 North Brand Boulevard, Suite 300, Glendale, CA 91203
[2] LOGICON RDA, 6053 West Century Boulevard, Los Angeles, CA 90009

ABSTRACT

Lagrangian finite element codes with explicit time integration are extensively used for the analysis of structures subjected to explosive loading. Within these codes, numerous material models have been implemented. However, the development of a realistic but efficient concrete material model has proven complex and challenging.

The plasticity concrete material model in the Lagrangian finite element code DYNA3D was assessed and enhanced. In the first phase, the main modifications included the implementation of a third, independent yield failure surface; removal of the tensile cutoff and extension of the plasticity model in tension; shift of the pressure cutoff; implementation of a three invariant formulation for the failure surfaces; determination of the triaxial extension to triaxial compression ratio as a function of pressure; shear modulus correction; and implementation of a radial path strain rate enhancement. These modifications insure that the response follows experimental observations for standard uniaxial, biaxial and triaxial tests in both tension and compression, as shown via single element analyses. The radial path strain rate enhancement insures constant enhancement for all those tests. As a full scale example, a standard dividing wall subjected to a blast load is analyzed and the effects of the modifications assessed.

Concrete subjected to shear stresses has been observed to dilate in the direction transverse to the shear stress plane. For reinforced concrete walls or slabs with in-plane restraints this can result in significant increases in load resistance due to arching. In a second phase of the material model development shear dilation was implemented. This latest model was used to model concrete cylinders wrapped with composite materials.

INTRODUCTION

In the analysis of complex structures subjected to blast loading and large deformations, Lagrangian finite element codes with explicit time integration have become a necessary and efficient tool [1]. In these codes a limited element library including trusses, beams, shells and solids has proven sufficient. However extensive material libraries have been required for

representation of the vast range of material behaviors. In the case of reinforced concrete structures, implementation of a realistic but efficient concrete material model has proven complex.

Numerous analyses for prediction of small and full scale blast tests of reinforced concrete structures sponsored by the Defense Nuclear Agency have provided an opportunity to revisit the existing material models in the finite element code DYNA3D [1,2,3]. The models potentially suitable for representing concrete's constitutive behavior were assessed over the full range from elastic response to failure. The most robust one, material model 16, still contains several shortcomings. In this report those deficiencies and the corresponding corrections are described.

ORIGINAL MATERIAL MODEL

The Lagrangian finite element code DYNA3D was originally developed by the Lawrence Livermore National Laboratory (LLNL) [1]. Within DYNA3D, several material models have been used in the past to represent concrete, namely material models 5 (Soil and Crushable Foam), 16 (Concrete/Geological Material), 17 (Isotropic Elastic-Plastic with Oriented Cracks), 25 (Extended Two Invariant Geologic Cap). Materials 5, 17 and 25 have exhibited significant limitations in modeling concrete behavior [4]. Material model 16, however, appeared more appropriate and presented some attractive features which could be easily enhanced.

OVERVIEW

The original material model 16 (subroutine f3dm16.f) decouples the volumetric and deviatoric responses. An equation of state gives the current pressure as a function of current and previous minimum (most compressive) volumetric strain. Once the pressure is known, a moveable surface - herein denominated a *yield* or *failure* surface - limits the second invariant of the deviatoric stress tensor. The volumetric response is easily captured via a tabulated input such as the one in equation of state 8. No changes were deemed necessary for this part of the response. However, the deviatoric response did present some shortcomings which were addressed. For example, due to the decoupling of volumetric and deviatoric responses, this original model has the limitation of not incorporating shear dilation which is observed with concrete. For the case of significant structural lateral restraints and low damage levels this may result in responses softer than expected.

During initial loading or reloading, the deviatoric stresses remain elastic until the stress point reaches the initial yield surface. The deviatoric stresses can then further increase until the maximum yield surface is reached. Beyond this stage the response can be perfectly plastic or soften to the residual yield surface (see Figure 1). Whenever the stress point is on the yield surface and the stress increment corresponds to loading on that surface, plastic flow occurs in accordance with a Prandtl-Reuss (volume preserving) flow rule, implemented by the well known "radial return" algorithm. The model also incorporates a tensile cutoff and a pressure cutoff.

ORIGINAL DEVIATORIC RESPONSE

Stress Limits

The function $\Delta\sigma$ which limits the deviatoric stresses is defined as a linear combination of two fixed three-parameter functions of pressure:

$$\Delta\sigma = \eta\Delta\sigma_m + (1-\eta)\Delta\sigma_r$$

$$\Delta\sigma_m = a_0 + \frac{p}{a_1 + a_2 p} \quad \text{(maximum stress difference)} \quad ,$$

where

$$\Delta\sigma_r = a_{0f} + \frac{p}{a_{1_f} + a_2 p} \quad \text{(residual stress difference)} \quad ,$$

and where $p = -(\sigma_{xx} + \sigma_{yy} + \sigma_{zz})/3$ is the pressure (stresses are positive in tension, pressure is positive in compression). The parameter η is a user-defined function of a modified effective plastic strain measure λ. The function $\eta(\lambda)$ is intended to first increase from some initial value up to unity, then decrease to zero representing softening. Hence, the yield surface migrates between $\Delta\sigma_r$, representing the minimum or residual strength, and $\Delta\sigma_m$, the maximum strength. The initial yield surface is given by

$$\Delta\sigma_y = \eta_y\Delta\sigma_m + (1-\eta_y)\Delta\sigma_r$$

where $\eta_y = \eta(0)$ is the initial value of η.

Available triaxial compression concrete data indicate that for the initial yield surface the principal stress difference $\Delta\sigma_y$ should be about 45% of the maximum stress difference. On the other hand, the residual strength should vanish for the unconfined compression test. Furthermore, because the two fixed surfaces become parallel for large values of *p*, they cannot properly represent the brittle-ductile transition point. The original formulation, with the constraint that the initial, maximum, and residual yield surfaces be linearly related, cannot properly capture the experimental data. This suggests the need for a third fixed yield surface independent from the other two.

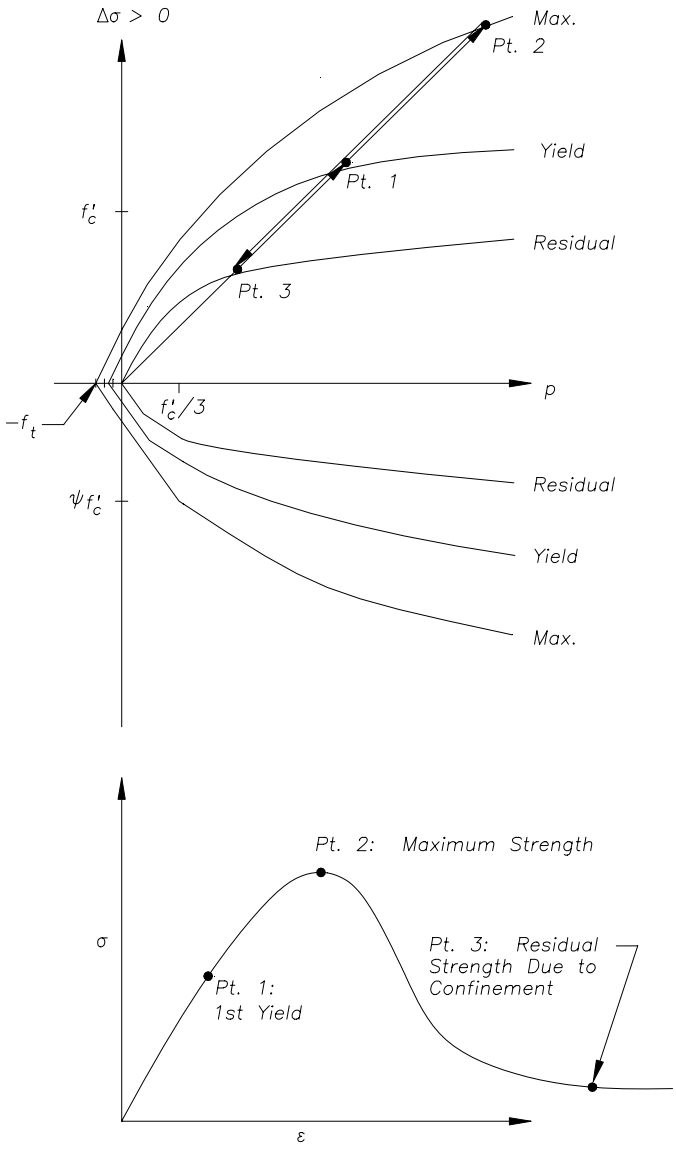

Figure 1. Three failure surfaces.

Compressive Meridian

Data for the compressive meridian are usually obtained from an unconfined compression test and triaxial compression tests with various levels of confinement. For the original model 16, a minimum of two nonzero levels of confinement are needed since three parameters define the

compressive meridian. The usual tests provide no data for pressures below $f_c'/3$ (failure in an unconfined compression test). The three-parameter maximum failure surface just described will usually overestimate the strength when extrapolated to pressures below $f_c'/3$. Similarly this formulation would overestimate the principal stress difference for the biaxial tension test.

Tensile Meridian

The tensile or extension meridian of the failure surface for concrete is usually lower (closer to the hydrostat at the same pressure) than the compressive meridian. Experimental data suggest that the ratio of the tensile to compressive meridian, herein denoted ψ, varies from about 0.5 at negative (tensile) pressures to unity at high confinements. Using equal meridians at low pressures will yield erroneous results (see Figure 2).

Tensile Cutoff

In an attempt to alleviate the previously noted shortcoming at low pressures, the original material model incorporates a tensile cutoff which limits the maximum principal stress to the tensile strength f_t (see Figure 2). For intermediate pressures $(0 < p < f_c'/3)$ this does not solve the problem. In addition the tensile cutoff algorithm reduces the current stress state to zero in 20 steps. This arbitrary and abrupt stress decrease contrasts with the smooth decay offered by the plasticity model when transitioning between the maximum and residual failure surfaces.

Pressure Cutoff

The original model also incorporates a pressure cutoff which prevents the pressure from going below $f_t/3$ (Figure 2). Although this does not affect the uniaxial tensile test, it does limit the principal stress difference to $f_t/2$ for a biaxial tensile test, and to $f_t/3$ for a triaxial tensile test. These limits disagree with experimental data showing that in both cases the principal stress difference should reach approximately f_t. In addition, whenever the pressure cutoff is

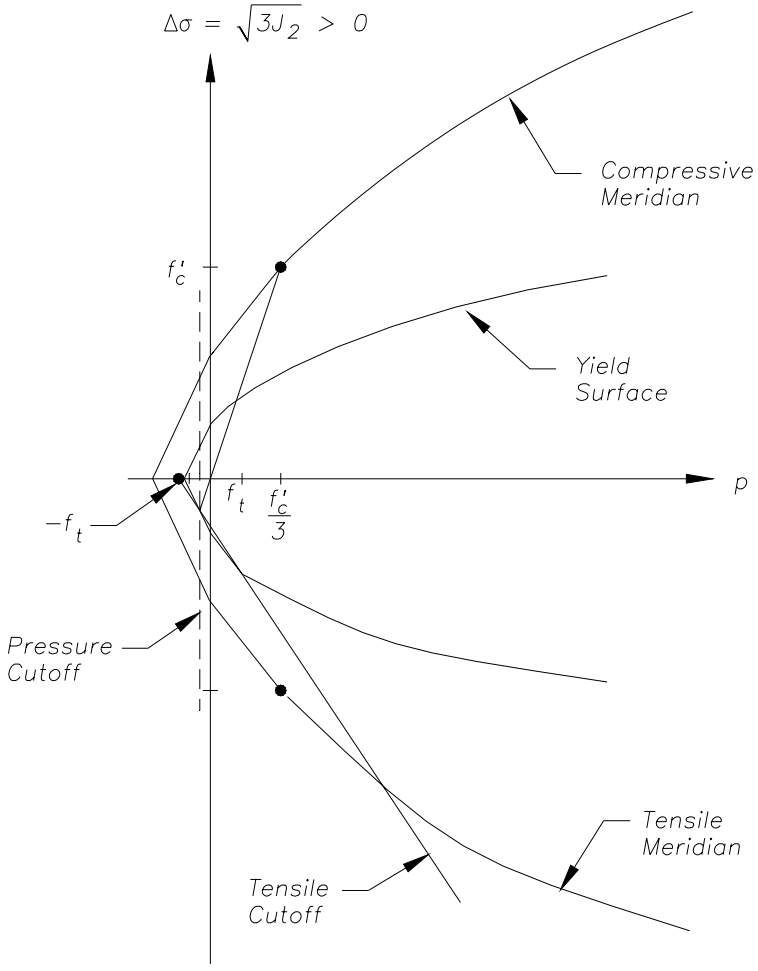

Figure 2. Original LLNL-DYNA3D failure surfaces.

reached in the original model, the current state of stress is maintained and no stress decay takes place upon further straining.

Rate Enhancement

In the original model, at any given *pressure*, the failure surfaces are expanded by a rate enhancement factor which depends on the effective deviatoric strain rate. Enhancing strength at a given pressure is inconvenient, because the rate enhancement factors available in the literature apply to the uniaxial unconfined compression and extension paths, not to a pure shear path. It is possible to derive the following formula to relate the test data to the input data in compression:

$$r_c = \frac{3a_1 f_c' r_f + a_2 f_c'^2 r_f^2}{3a_0 a_1 + (1 + a_0 a_2) f_c' r_f}$$

where r_c = input to DYNA3D (rate enhancement factor at fixed pressure), and r_f = experimental rate enhancement factor from an unconfined uniaxial compression test. However the original program uses the same factor for enhancing stress states at negative pressures. When calibrated to unconfined compression, this results in almost no enhancement for the uniaxial tension test.

Elastic Behavior

The original LLNL material model 16 has two options for the elastic response, both isotropic. Both use the bulk modulus from the pressure-volume relation to compute a second elastic constant. One assumes a constant Poisson's ratio, the other a constant shear modulus. Although a constant shear modulus absolutely guarantees that no elastic energy can be generated, that option was dropped due to its inadequacy to represent known data. In the other option, the user specifies a value of Poisson's ratio. When used with equation of state 8, the model derives a shear modulus from the current *unloading* bulk modulus. This method easily leads to inconsistencies such as negative Poisson ratios upon initial loading [5]. The assumption of constant Poisson's ratio was retained, but the computation of the shear modulus was modified.

ENHANCED PRANDTL-REUSS MATERIAL MODEL

The original material model 16 was significantly modified to correct most of the shortcomings noted in the previous section.

NEW PRESSURE CUTOFF

The pressure cutoff p_c now has an initial value of $-f_t$ (see Figure 3). Together with changes in the maximum failure surface described below, both the biaxial and triaxial tensile tests can now reach a principal stress difference of f_t.

Upon failure in the negative pressure range, the parameter η is used not only to reduce the current failure surface from the maximum to the residual, but also to increase the pressure cutoff from $-f_t$ to zero in a smooth fashion. This is done by checking the pressure returned by the equation of state subroutine, and resetting it to p_c if it violates $p \geq p_c$, where

$$p_c = \begin{cases} -\mathrm{f_t} \text{ if the maximum failure surface has not been reached (hardening)} , \\ -\eta \mathrm{f_t} \text{ otherwise (softening)} . \end{cases}$$

Note that although implemented in the concrete material model subroutine, this modification can override the pressure calculated in the equation of state. This pressure cutoff is necessary as otherwise the equation of state would calculate very large negative pressures for large volumetric extensions beyond cracking, which would be physically incorrect.

COMPRESSIVE MERIDIANS OF THE FIXED FAILURE SURFACES

A third, independent, fixed surface has been implemented with three new parameters (a_{0y}, a_{1y}, a_{2y}). This surface represents initial yielding and is given by

$$\Delta\sigma_y = a_{0y} + \frac{p}{a_{1y} + a_{2y} p} \quad .$$

Since for concrete the residual strength in tension is zero, the pressure independent parameter in the formulation of the residual surface is not needed, i.e., $a_{0f} = 0$. To permit the residual and the maximum failure surfaces to intersect at a point representing the brittle-ductile transition, a new parameter a_{2f} has been added. The residual surface now takes the form

$$\Delta\sigma_r = \frac{p}{a_{1f} + a_{2f} p}$$

In the new model, after reaching the initial yield surface but before the maximum failure surface, the current surface is obtained as a linear interpolation between the two:

$$\Delta\sigma = \eta(\Delta\sigma_m - \Delta\sigma_y) + \Delta\sigma_y$$

where η varies from 0 to 1 depending on the accumulated effective plastic strain parameter λ. After reaching the maximum surface the current failure surface is similarly interpolated between maximum and residual:

$$\Delta\sigma = \eta(\Delta\sigma_m - \Delta\sigma_r) + \Delta\sigma_r$$

The function $\eta(\lambda)$ is input by the user as a series of (η, λ) pairs. This function would normally begin at 0 at λ=0 , increase to 1 at some value $\lambda=\lambda_m$, and then decrease to 0 at some larger value of λ . Since λ is non-decreasing, this would permit Δσ sequentially to take on the values

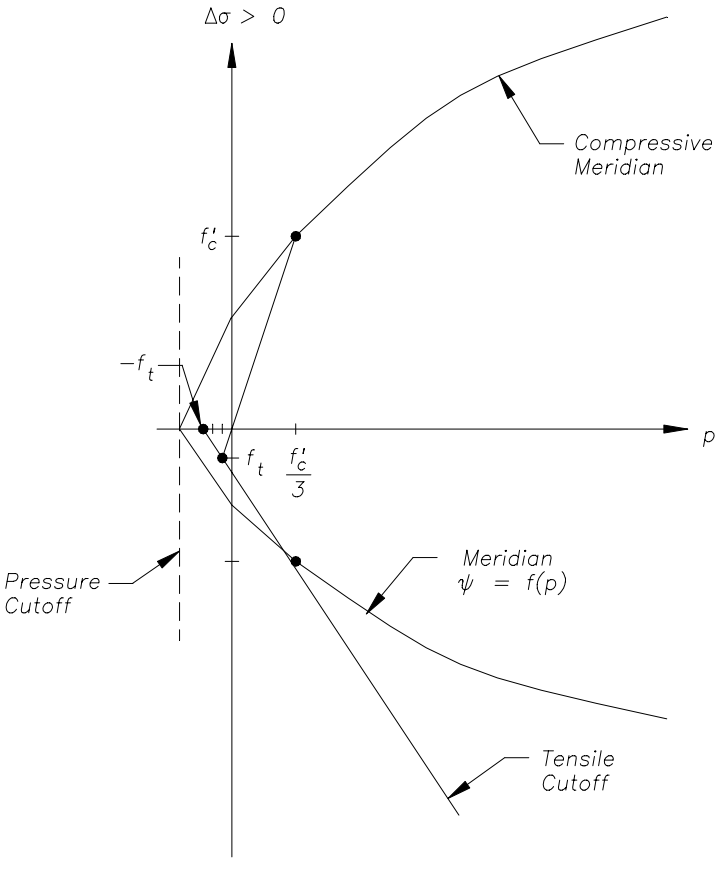

Figure 3. Willam Warnke failure surface.

$\Delta\sigma_y$, $\Delta\sigma_m$, and $\Delta\sigma_f$. In fact, there are no internal checks to guarantee that the user's input takes on these specific values. Thus, at the beginning of the subroutine the value of λ_m is defined simply as the value of λ corresponding to the first relative maximum of η in the input table. Then, whenever $\lambda \le \lambda_m$ the current surface is interpolated between the initial yield and the maximum; conversely, if $\lambda > \lambda_m$ the current surface is interpolated between the maximum and the residual. In summary a total eight parameters define the three fixed surfaces, as follows:

$$\Delta\sigma_m = a_0 + \frac{p}{a_1 + a_2 p} \qquad \text{(maximum failure surface)} \ ,$$

$$\Delta\sigma_r = \frac{p}{a_{1f} + a_{2f} p} \qquad \text{(residual failure surface)} \ ,$$

$$\Delta\sigma_y = a_{0y} + \frac{p}{a_{1y} + a_{2y} p} \qquad \text{(yield failure surface)} \ .$$

At pressures above the brittle-ductile transition, $\Delta\sigma_r$ should be limited to $\Delta\sigma_m$. In the code this is ensured by resetting $\Delta\sigma_r$ to $\Delta\sigma_m(p)$ if $\Delta\sigma_r$ from the nominal formula exceeds $\Delta\sigma_m(p)$. The yield surface is similarly limited to $\Delta\sigma_m$ [2].

DAMAGE ACCUMULATION

New Shear Damage Accumulation

The current failure surface is interpolated from the maximum failure surface and either the yield or the residual failure surface as

$$\Delta\sigma = \eta(\Delta\sigma_m - \Delta\sigma_{min}) + \Delta\sigma_{min}$$

where $\Delta\sigma_{min}$ is either $\Delta\sigma_y$ or $\Delta\sigma_r$ depending on whether $\lambda \le \lambda_m$ or $\lambda > \lambda_m$, and where η is a function of λ . In the original model 16, the modified effective plastic strain λ , is defined as

$$\lambda = \int_0^{\overline{\varepsilon^p}} \frac{d\overline{\varepsilon^p}}{\left(1 + p / \mathrm{f_t}\right)^{b_1}}$$

where the effective plastic strain increment is given by $d\overline{\varepsilon^p} = \sqrt{(2/3)\varepsilon_{ij}^p \varepsilon_{ij}^p}$.

In the new model, two changes have been implemented. First rate effects were included, and second, the parameter b_1 is replaced by b_2 for tensile pressure (p<0), as follows:

$$\lambda = \int_0^{\overline{\varepsilon^p}} \frac{d\overline{\varepsilon^p}}{r_f\left(1 + p / r_f \mathrm{f_t}\right)^{b_1}} \qquad \text{for } p \ge 0$$

$$\lambda = \int_0^{\overline{\varepsilon^p}} \frac{d\overline{\varepsilon^p}}{r_f\left(1 + p / r_f \mathrm{f_t}\right)^{b_2}} \qquad \text{for } p < 0$$

Note that at p = 0, the denominator is a continuous function. In this way, the damage evolution can be different in tension and compression, if needed.

Volumetric Damage

With damage accumulation as just described, if a triaxial tensile test is modelled, wherein the pressure decreases from 0 to $-f_t$ with no deviators, then no damage accumulation occurs. The parameter λ remains 0 and so does η. The equation of state decreases the pressure to $-f_t$ but keeps it at that level thereafter. To implement a pressure decay after tensile failure, a volumetric damage increment can be added to the deviatoric damage whenever the stress path is "close" to the triaxial tensile test path, i.e., the negative hydrostatic axis. The closeness to this path is measured by the ratio $\left|\sqrt{3J_2}\ /\ p\right|$, which, for example, is 1.5 for the biaxial tensile test. To limit the effects of this change to the paths close to the triaxial tensile path, the incremental damage is multiplied by a factor f_d given by $f_d = 1 - \left|\sqrt{3J_2}\ /\ p\right| * 10 \quad for \quad 0 \le \left|\sqrt{3J_2}\ /\ p\right| < 0.1$, 0 otherwise. The modified effective plastic strain is incremented by $\Delta\lambda = b_3 f_d k_d (\varepsilon_v - \varepsilon_{v,yield})$ where b_3 = input scalar multiplier, k_d = internal scalar multiplier, ε_v = volumetric strain, and $\varepsilon_{v,yield}$ = volumetric strain at yield.

Determination of Damage Evolution Parameters b_2 and b_3

The values of b_2 and b_3 govern the softening part of the unconfined uniaxial tension stress-strain curve as the stress point moves from the maximum to the residual failure surfaces. It is well known that, unless such softening is governed by a localization limiter or characteristic length, the results will not be objective upon mesh refinement, i.e. they will be mesh-dependent. One way to eliminate this mesh dependency is to force the area under the stress-strain curve to be G_f/h, where G_f = fracture energy and h = a characteristic length, which may be associated with a localization width. The fracture energy usually varies from 40 to 175 N/m (0.23 to 1

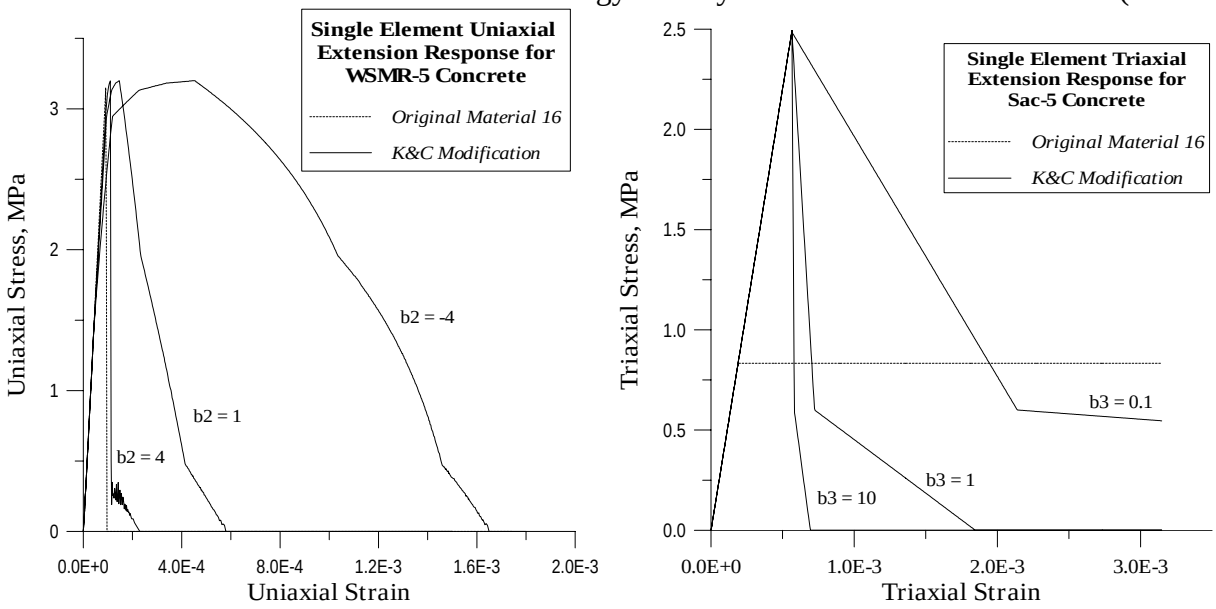

(a) Parameter b_2: effect on uniaxial tension strain softening.

(b) Parameter b_3: effect on triaxial tensile strain softening.

Figure 4. Effects of parameters b_2 and b_3 on tension softening.

lbf/in) according to the European CEB-FIP model code (Section 2.1.3.3.2: Fracture Energy) [6].

In a typical analysis, a localization width (width of the localization path transverse to the crack advance) is chosen together with G_f, and b_2 and b_3 are determined by iterative calculations. An example of the effects of b_2 and b_3 on the stress-strain response of a single element subjected to uniaxial and triaxial tensile tests is shown in Figure 4. If the analysis yields a different localization width than anticipated, this should be corrected and the calculation restarted. These parameters will be of importance when the structure analyzed is lightly reinforced or is tension- or shear- critical. In dynamic analyses the localization pattern may vary during the run, depending on the relative amount of damping. The localization width can vary from one to several element widths. Similar considerations should be brought to bear when selecting a value for b_1 , which governs softening in compression.

THREE-INVARIANT FAILURE SURFACE FORMULATION

Development of a Three-Invariant Model

The previous $\Delta\sigma$ versus p relationships actually define only the compressive meridians of the failure surfaces in principal stress space. The original material model 16 assumes the full failure surfaces are obtained by rotating these meridians around the hydrostatic axis, thereby forming circular cross sections in the deviatoric planes. The surfaces are functions of pressure and the second invariant of the deviatoric stress tensor, J_2 , whose square root is proportional to the radius of the circle. A third invariant, such as J_3 or Lode angle θ (angular offset in the deviatoric plane of the stress point from the image of a positive, i.e. tensile, principal stress axis) may be introduced to permit more general shapes in the deviatoric plane, such as the triangular curves with smooth corners shown in Figure 5a. For concrete the deviatoric section typically transitions from this shape at low pressures to circular at high pressures. Figures 5b and 5c show the large difference that can exist between the tensile and compressive meridians. Moreover, the difference is amplified when considering failure levels under compressive, proportional loadings, represented by rays emanating from the origin in stress space. These differences can be captured in the model only if a third invariant is included.

To introduce the third invariant, a dependence on the Lode angle θ (Figure 6a) is sought. The shape proposed by Willam and Warnke [7] is adopted, providing a smooth, convex triangular surface generated by elliptical segments as shown in Figure 6b. If r_c is the distance from the hydrostatic axis to the failure surface at the compressive meridian, and r_t the distance at the tensile meridian, then at any intermediate position the distance r ($r_t < r < r_c$) will be given by

$$r = \frac{2r_c\left(r_c^2 - r_t^2\right)\cos\theta + r_c\left(2r_t - r_c\right)\sqrt{4\left(r_c^2 - r_t^2\right)\cos^2\theta + 5r_t^2 - 4r_t r_c}}{4\left(r_c^2 - r_t^2\right)\cos^2\theta + \left(r_c - 2r_t\right)^2} \quad .$$

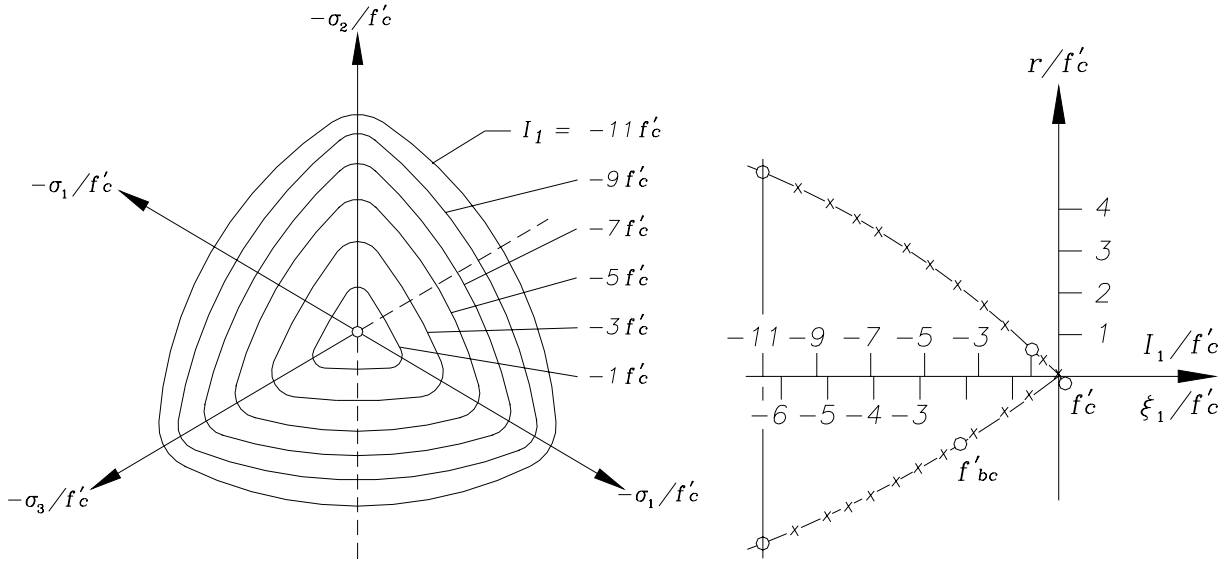

(a) Deviatoric sections for increasing pressure. (b) Hydrostatic section.

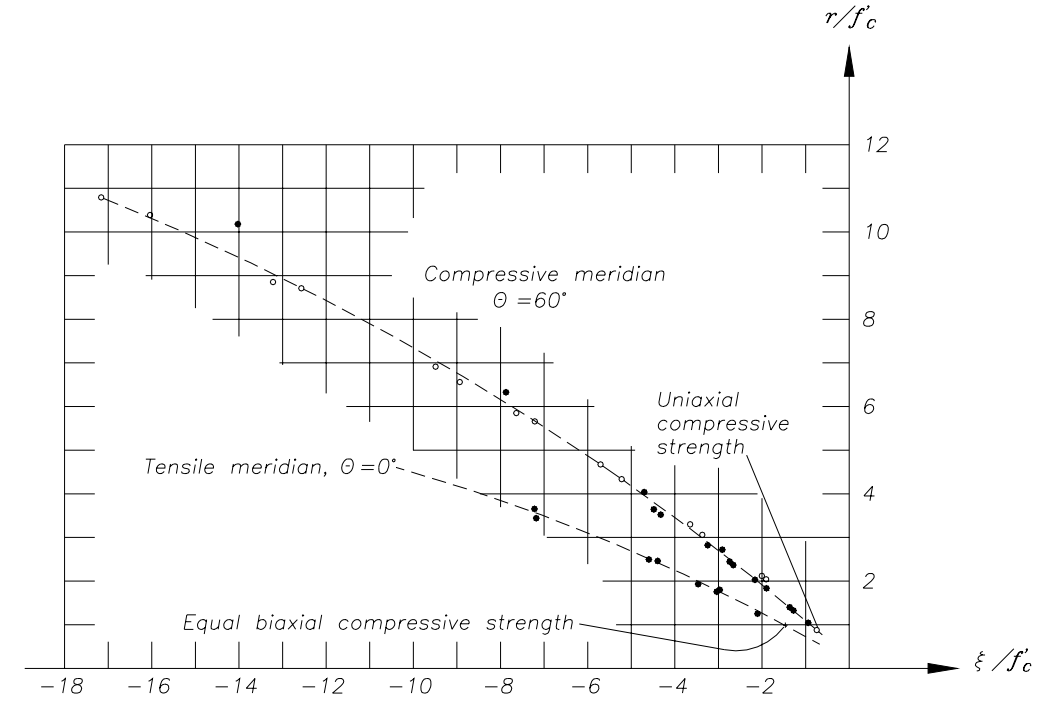

NOTE: $r = \sqrt{2J_2}$

$\xi = I_1/\sqrt{3}$

(c) Typical tensile and compressive meridians.

Figure 5. Typical failure surface section for concrete from [7].

By dividing both sides by r_c, then dividing the numerator and denominator of the right hand side by r_c^2, we obtain

$$r' = \frac{2\left(1-\psi^2\right)\cos\theta + \left(2\psi-1\right)\sqrt{4\left(1-\psi^2\right)\cos^2\theta + 5\psi^2 - 4\psi}}{4\left(1-\psi^2\right)\cos^2\theta + \left(1-2\psi\right)^2}$$

where $r' = r / r_c$ and $\psi = r_t / r_c$. Note that r' depends only on ψ and θ, and that in general ψ in turn depends on *p*. For θ = 0° the formula yields $r' = \psi$ corresponding to pure extension, and for θ = 60° it yields $r' = 1$ corresponding to pure compression. The value of θ can be obtained from

$$\cos\theta = \frac{\sqrt{3}}{2}\frac{s_1}{\sqrt{J_2}} \qquad \text{or} \qquad \cos 3\theta = \frac{3\sqrt{3}}{2}\frac{J_3}{J_2^{3/2}}$$

where s_1 = first principal deviatoric stress = $\max\left[\sigma_1 - p,\ \sigma_2 - p,\ \sigma_3 - p\right]$, ($\sigma_1$, σ_2, σ_3) are the principal stresses, and the stress invariants J_2 and J_3 are given by

$$J_2 = \frac{1}{2}\left(s_1^2 + s_2^2 + s_3^2\right), \quad J_3 = s_1 s_2 s_3 = \begin{vmatrix} s_x & \tau_{xy} & \tau_{xz} \\ \tau_{yx} & s_y & \tau_{yz} \\ \tau_{zx} & \tau_{zy} & s_z \end{vmatrix} .$$

Once the value of r' is known, the original compressive meridians are multiplied by it to obtain the meridian at that location.

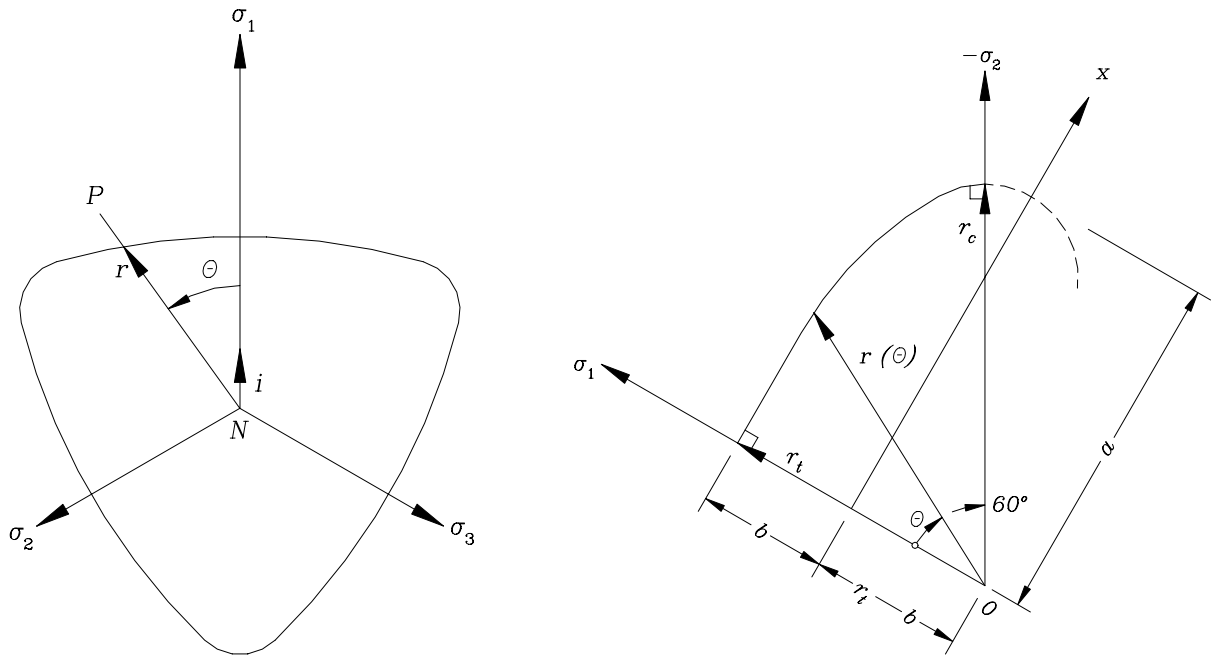

(a) Angle of similarity θ. (b) Elliptical approximation for 0 < θ < 60.

Figure 6. Deviatoric plan section in the Willam Warnke model adopted from [7].

Migration Between Fixed Failure Surfaces in Triaxial Extension

Lacking guidance from laboratory data, the transition between fixed failure surfaces in triaxial extension was taken to be the same as in triaxial compression. This transition is given by the λ-η relationship, which has been discussed in sections 3.3.1-2. If a different transition were found for the triaxial extension cases, then a second, independent λ–η relationship would have to be implemented.

New Compressive Meridian

Up to this point in the development it was implied that the compressive meridian is known and input to the code, and the extension meridian can be found as a fraction ψ of the compression one. In fact, depending on data availability, in some pressure ranges it is more appropriate to define the tensile meridian, and then obtain the compressive meridian from the tensile one. The specification built into the new model results from a combination of both approaches, as described here and in the following subsections.

For pressures in excess of $f_c'/3$, the input compressive meridian (determined by the parameters a_0, a_1 and a_2) does serve as a basis for all the others.

For pressures below $f_c'/3$ and above $-f_t$, we limit the maximum tensile stress on the extension meridian to f_t . This uniquely defines the extension meridian as $\Delta\sigma = 1.5\,(p + f_t)$ which passes through both the triaxial tensile test failure point at (p, Δσ) = ($-f_t$, 0) and the uniaxial tensile test point at (p, Δσ) = ($-f_t/3$, f_t) . At $p = f_c'/3$ the two formulations are forced to coincide by determining the appropriate value of ψ. The compressive meridian for pressures less than $f_c'/3$ then follows as the image of the tensile meridian, i.e., the tensile meridian divided by ψ(p) at each pressure p. The following subsections describe the determination of ψ(p) in detail. All three compression failure surfaces (yield, maximum, residual) have corresponding tensile images.

Given this segmental failure surface formulation and the piecewise linear definition of ψ as a function of pressure, the failure surface will not be smooth. This does not violate any fundamental theoretical requirement. In fact, due to the use of a Prandtl-Reuss flow rule as implemented with the "radial return" algorithm, it creates no numerical difficulties either.

Definition of ψ(p)

To complete the implementation of the three-invariant failure surface, the function ψ(p) has to be defined for the full range of possible pressures.

As mentioned earlier, for concrete ψ varies from 1/2 at negative (tensile) pressures to unity at high compressive pressures. In order to satisfy various observations for specific triaxial stress paths, the values of ψ are preset within the code for several pressures, as follows.

Case $p \le 0$ (tensile pressure). For $p \le 0$ the tensile meridian has to include the points (p, -Δσ) = ($-f_t$, 0) and (p,-Δσ) = ($-f_t/3$, f_t), which represent failure in triaxial and uniaxial tensile tests respectively. At $p = -2f_t/3$ the compressive meridian is

$$\frac{\Delta\sigma}{\psi} = \frac{3}{2}\left(\frac{-2f_t}{3} + f_t\right)\frac{1}{\psi} = \frac{f_t}{2\psi} \quad .$$

However, this should represent failure in the biaxial tensile test, which test data suggest is approximately given by $\Delta\sigma = f_t$. By equating both stress differences, $\psi = 1/2$ at $p = -2f_t/3$.

Another test of interest is the pure shear test in plane stress. If the coordinates are rotated 45° in plane, the resulting state of stress is $(\sigma_1, \sigma_2, \sigma_3) = (\tau, 0, -\tau)$. Assuming that the maximum tensile stress is limited by f_t, then $\tau = f_t$ at failure. From $(\sigma_1, \sigma_2, \sigma_3)$, $\Delta\sigma$ can be found as:

$$\Delta\sigma = \sqrt{3J_2} = \sqrt{3}f_t \quad .$$

For this test, the principal stress difference is given by r' times the compressive meridian, i.e.

$$\Delta\sigma = r'\frac{3(p + f_t)}{2\psi} = r'\frac{3f_t}{2\psi}$$

with $r' = r'(\psi, \theta = 30^\circ)$. The two expressions are equal provided $\psi = 1/2$ at $p = 0$, because $r'(1/2\ , 30) = 1/\sqrt{3}$. Thus uniaxial, biaxial, and triaxial tensile failure and pure shear failure can all be plausibly represented with $\psi = 1/2$ for $p \le 0$. For example, this gives the nominal maximum compressive failure surface the form $\Delta\sigma_m = 3(p+f_t)$.

Case $p = f'_c/3$ (unconfined compression test). At $p = f'_c/3$, the uniaxial unconfined compressive test yields a principal stress difference of f'_c. The corresponding point on the extension meridian is $\Delta\sigma = \psi f'_c$. This should be equal to the defined extension meridian (Figure 7)

$$\Delta\sigma = \frac{3}{2}(p + f_t) = \frac{3}{2}\left(\frac{f'_c}{3} + f_t\right)$$

hence

$$\Psi = \frac{1}{2} + \frac{3}{2}\frac{f_t}{f'_c} \ .$$

This expression actually represents an upper limit for ψ. For example, if $f_t/f'_c = 0.10$ (typical of concretes with $f'_c \le 5000$ psi) then $\psi = 0.65$.

Case $p = 2\alpha f'_c/3$ (biaxial compression test). Biaxial compression tests conducted by Kupfer et al. [8] have shown failure occurring at $(\sigma_1, \sigma_2, \sigma_3) = (0, \alpha f'_c, \alpha f'_c)$ with $\alpha \approx 1.15$. The stress point lies on the tensile meridian at a pressure $p = 2\alpha f'_c/3 \approx 2.3f'_c/3$ and a stress difference $|\Delta\sigma_{tm}| = \alpha f'_c$. The corresponding point on the compressive

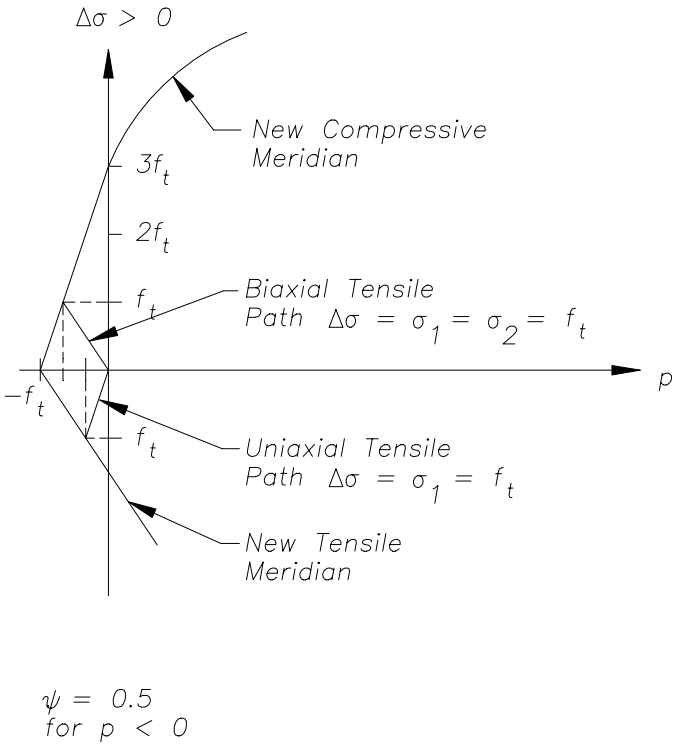

Figure 7. Derivation of ψ for $p < 0$.

meridian is given in terms of the input parameters as

$$\Delta\sigma_{cm} = a_0 + \frac{p}{a_1 + a_2 p} = a_0 + \frac{2\alpha\ \mathrm{f}_c'/3}{a_1 + a_2(2\alpha\ \mathrm{f}_c'/3)} \quad ,$$

so the ratio $\psi = \left|\Delta\sigma_{tm} / \Delta\sigma_{cm}\right|$ is

$$\psi = \frac{\alpha\ \mathrm{f}_c'}{a_0 + \dfrac{2\alpha\ \mathrm{f}_c'/3}{a_1 + 2a_2\,\alpha\ \mathrm{f}_c'/3}} \qquad \text{with } \alpha = 1.15$$

Completion of definition of ψ. For computational purposes, the function $\psi(p)$ is piecewise linear, using the previously defined values. For higher compression pressures, two additional data points from existing databases were chosen, as follows:

$$\psi = 0.753 \qquad \text{at } p = 3\mathrm{f}_c' \quad ,$$

$$\psi = 1 \qquad \text{for } p \geq 8.45\mathrm{f}_c' \quad .$$

The last entry represents the transition point beyond which the tension and compression meridians are equal, and the failure surface becomes a circle in the deviatoric plane. In summary,

$$\psi(p) = \begin{cases} 1/2\ , & p \leq 0\ , \\ 1/2 + 3\mathrm{f}_t/2\mathrm{f}_c'\ , & p = \mathrm{f}_c'/3\ , \\ \dfrac{\alpha\mathrm{f}_c'}{a_0 + \dfrac{2\alpha\mathrm{f}_c'/3}{a_1 + 2a_2\alpha\mathrm{f}_c'/3}}\ , & p = 2\alpha\mathrm{f}_c'/3\ , \\ 0.753\ , & p = 3\mathrm{f}_c'\ , \\ 1\ , & p \geq 8.45\mathrm{f}_c'\ , \end{cases}$$

and the function is linear between the specified points.

Comparison with previously reported values of ψ. Based on various experimental data, Ahmad and Shah have proposed the following values for ψ [9]:

$$\psi = 0.686 \qquad \text{if} \quad 1/3 \leq p/\mathrm{f}_c' < 1.75 \quad ,$$

$$\psi = 0.61 + 0.0435\frac{p}{\mathrm{f}_c'} \quad \text{if} \quad 1.75 \leq p/\mathrm{f}_c' < 8.96$$

The proposed values of ψ for $p/\mathrm{f}_c' \geq 3$ are based on this and additional data for SAC5 concrete. For $p/\mathrm{f}_c' = 1/3$, using $\psi = 0.686$ implies that, in some cases and while unloading uniaxially from an isotropic compression state, the failure surface would only be reached for $\sigma_1 = 0.124\mathrm{f}_c'$. This would probably only happen for concretes with low compressive strengths

($f_c' \le 4000$ psi), where $f_t / f_c' \ge 0.10$. Based on several data sets, Chen [7] suggests that $\psi = 0.5$ for $p / f_c' \approx 0$, $\psi = 0.8$ for $p / f_c' \approx 7$.

RADIAL RATE ENHANCEMENT

Since in typical experiments rate enhancements are obtained along radial paths from the origin in the principal stress difference versus pressure plane (via unconfined compressive and tensile tests), strength enhancement was implemented in general along radial stress paths. This is accomplished as follows. Let r_f be the enhancement factor and p the pressure after calling the equation of state subroutine. The enhanced value $\Delta\sigma_e$ of the failure surface at pressure p is desired, assuming the enhancement factor is applied radially. To get $\Delta\sigma_e$ an "unenhanced" pressure p/r_f is first obtained, then the unenhanced strength $\Delta\sigma(p/r_f)$ is calculated for the specified failure surface. Finally the unenhanced strength is multiplied by the enhancement factor to give

$$\Delta\sigma_e = r_f \Delta\sigma(p / r_f)$$

This simple formulation presents the following advantages: (1) the code input is obtained directly from the test data at the same strain rate, and (2) strength is equally enhanced along any radial stress path, including uniaxial and biaxial tension and compression. This is far more consistent with data than the earlier formulation.

COMPRESSIVE MERIDIAN IN THE SOFTENING REGIME

Compressive Meridian For Negative Pressures

With the modifications discussed so far, if $p < 0$ and softening is underway, there will be a vertical segment in the current
failure surface (in the p versus $\Delta\sigma$ plane,) due to the reduction in minimum pressure p_c.. In other words, the current failure surface is given by

$$\Delta\sigma = \eta\ (\Delta\sigma_m - \Delta\sigma_r) + \Delta\sigma_r \quad \text{for } p > p_c$$

and a vertical segment at $p = p_c$..

To avoid this vertical segment but maintain the reduction in magnitude of p_c, a modified maximum failure surface $Y_1(p,\eta)$ can be defined as follows when pressure is negative and softening is under way ($\lambda > \lambda_m$):

$$Y_1(p,\eta) = Y_m(p) - \frac{p_f - p}{p_c - p_c(\eta)} Y_m(p_c) = 3\left(\frac{p}{\eta} + f_t\right)$$

where

Y_m = nominal maximum failure surface in compression = $3(p+f_t)$,

p_f = intersection of the residual surface with the pressure axis = 0 (for concrete),

$p_c(\eta) = \eta p_m + (1-\eta)\, p_f = \eta p_m$,

p_m = intersection of the maximum surface with the pressure axis = $-f_t$.

As defined, Y_1 is continuous with Y_m at $p = p_f = 0$. The current failure surface in the softening range can then be defined as follows:

$$Y(p,\eta) = \begin{cases} \eta\Delta\sigma_m(p) + (1-\eta)\Delta\sigma_f(p) \quad , & p > p_f \quad , \\ \eta Y_1(p,\eta) = \eta Y_m - \dfrac{p_f - p}{p_f - p_m} Y_m(p_c) = 3(p + \eta \mathrm{f_t}) & p \le p_f \quad . \end{cases}$$

The formula above is uncorrected for rate enhancement. The correction follows as outlined in Section 3.5. Given an updated pressure p (which implicitly includes effects of rate enhancement), the corresponding "unenhanced" state is denoted by $p_u = p/r_f$ where r_f is the enhancement factor. The current unenhanced failure surface for negative pressures can be written as

$$Y_u(p_u,\eta) \;=\; \eta Y_1(p/r_f\,,\;\eta) = 3\left(\frac{p}{r_f} + \eta \mathrm{f_t}\right) \quad \text{for} \quad p/r_f < p_f \quad (p_f = 0 \text{ for concrete})$$

The corresponding enhanced failure surface follows by multiplying by r_f:

$$Y_e(p,\eta) = r_f\left[\eta Y_m(p/r_f) - \frac{p_f - p/r_f}{p_f - p_m} Y_m(p_c)\right] = 3(p + \eta r_f \mathrm{f_t}) \quad .$$

Corrections to the Flow Rule

The foregoing modification has the undesirable effect of complicating the dependence of the failure surface on p and η. The expressions for the updated stresses and the increment dλ of the damage parameter must be also modified. The derivation, which is based on the assumption of Prandtl-Reuss (volume-preserving) plastic flow, is presented in Reference [2].

SHEAR MODULUS CORRECTION

With the constant Poisson's ratio option and equation of state 8, the original model 16 computes the elastic shear modulus from the specified constant Poisson's ratio and the current *unload/reload* bulk modulus. This can easily lead to a negative effective Poisson's ratio on loading whenever there is a large enough disparity between loading and unload/reload bulk moduli. In a first attempt at correcting this deficiency, the shear modulus was made dependent on whichever bulk modulus was currently in effect. However, this method failed because even infinitesimal pressure oscillations, for example during an unconfined compressive loading, led to large shear modulus oscillations which did not reflect the nominally continuously increasing load. In addition, these oscillations were encouraged by the fact that elastic energy could be generated whenever pressure increased while shear stress decreased.

A better approach is to compute the shear modulus based on a scaled bulk modulus, one which varies from the loading to the unload/reload value depending on how far the pressure is below the virgin curve. A scaling factor which varies from zero to unity as pressure drops from the virgin loading curve to p_f is given by

$$\varphi \;=\; \frac{-\Delta\varepsilon}{-\Delta\varepsilon + (p - p_f)/K_U}$$

where $\Delta\varepsilon = \varepsilon_{v,\min} - \varepsilon_v$, ε_v is volumetric strain, and K_U is the unload/reload bulk modulus from equation of state 8. If K_L is the corresponding loading modulus, the scaled bulk modulus is

$$K' = (K_L - K_U)\, e^{-5.55\varphi} + K_U$$

where the constant 5.55 is chosen so that K' will increase half way to the unload/reload value when p has dropped 1/8 of the way from the virgin curve to p_f. The shear modulus is then calculated as

$$G = (1.5 - 3\nu)\, K' / (1+ \nu)$$

APPLICATION EXAMPLE: SUBSTANTIAL DIVIDING WALLS

Substantial dividing walls (SDW's) in munitions production, maintenance, and storage facilities are used to subdivide explosives to prevent sympathetic detonation and to provide operational shields for personnel. They are 12 inch thick concrete walls with #4 reinforcing bars at 12 inch spacings on each face and in each direction, and without any shear reinforcing. Current Army and Air Force safety regulations assume that the 12 inch SDW's will prevent propagation for up to 425 pounds of Class/Division 1.1 explosives. This example was initially analyzed to provide a verification of the propagation prevention limits of the 12 inch SDW [10].

Although both the mass and velocity of secondary fragments are used for their capability of detonating the acceptor charge, only their velocity is estimated in this example. This is due to the difficulty for current analytical models to provide reliable estimates of fragment sizes. Established criteria indicates expected velocities of 400 to 500 feet per second for typical fragment sizes.

LOAD DEFINITION

Definition of airblast loadings was performed using two widely used Navy codes: SHOCK [11] to produce the shock loading (early time airblast) resulting from the incident blast wave and FRANG [12] to compute the gas pressure (late time airblast) resulting from expansion of the detonation products and heating of the air within the room. The process adopted was to compute loads independently of the response of the wall, *i.e.*, the walls were assumed to be rigid. The assumption of rigid boundary conditions is considered reasonable for this set of problems because the shock pressure pulse lasts less than a millisecond, in which time the wall has not yet moved significantly.

TEST DESCRIPTION

A description of the selected test (C6) and the relevant design data was obtained from Reference [13]. This experiment was conducted in the early 1960's at the Naval Ordnance Test Station (NOTS) in China Lake, California and consisted of a cased donor munition placed within a cubicle with three side walls (no roof) with numerous acceptor charges placed immediately outside the dividing walls. The charge (272 lbs) was detonated, resulting in complete destruction

of the dividing wall but no sympathetic detonations. Data from Reference [13] indicates that C-6 fragments were measured at a velocity of 500 ft/sec.

Table 1. Summary of steel properties.

	Yield Stress (ksi)		Ultimate Stress (ksi)		Fracture Strain
Steel Grade	Static	High Rate	Static	High Rate	(%)
40	40	52	110	128	12
60	69	90	131	153	11

STRUCTURAL MODEL

The discretization used to represent a typical SDW in the parametric calculations is shown in Figure 8, which illustrates a model with three supported sides (one side wall is frangible). The model for a wall with two supported sides (roof is also frangible) is similar, except that the stub along the roof line is omitted. In both cases no significant in-plane restraints exist for the walls, hence no significant effects from shear dilation are expected. The selected mesh has 6 brick elements through the thickness for the concrete, one for the cover on each side and four inside the rebar cage. Reinforcing steel was modeled using truss elements at 12 inch spacings in each direction. The model used for steel, identified in DYNA3D as Material 19, has similar features to the concrete model: inclusion of strain rate effects, non-linear post-yield hardening, and failure upon reaching a pre-defined level of strain. This last property is essential as bar failure is observed in each one of the runs performed, and without accurate representation

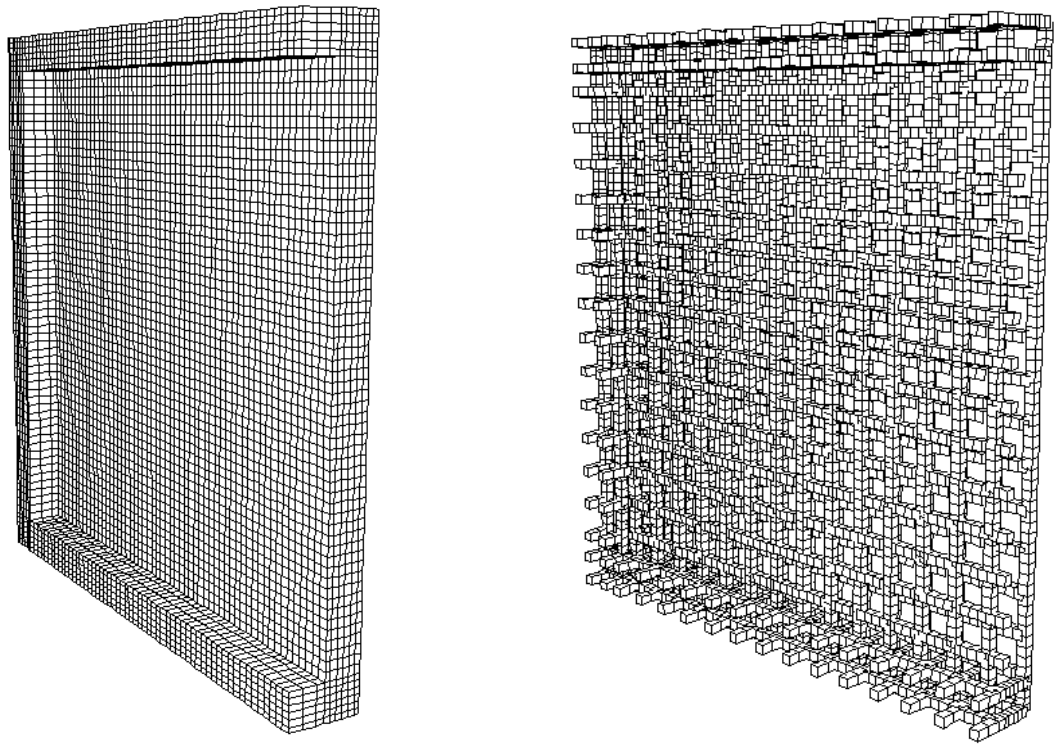

Figure 8. View of DYNA3D concrete and steel meshes (3-sided support).

of the breakage of reinforcing bars, the resulting secondary fragment velocity could not be adequately predicted. An example of the stress strain curves required as input for this material is presented in Figure 9: one for static properties, one for infinite rate (limit case), and one for an intermediate value at which properties have been measured (see also Table 1). This allows independent scaling of yield and ultimate strengths as a function of strain rate.

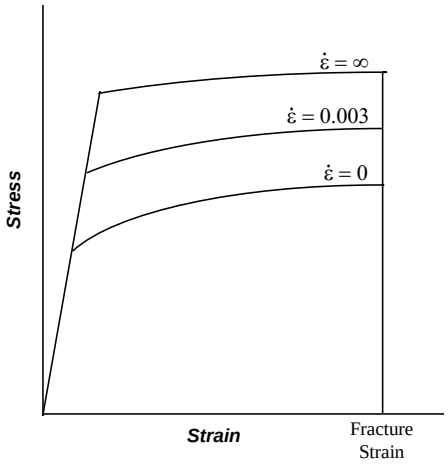

Figure 9. Inputs to material 19 (steel).

ANALYTICAL PREDICTIONS VERSUS TEST RESULTS FOR TEST C-6

Two runs were performed for this case to assess the desirability of using finer meshes, one with a 2-inch element size (fine) and one with a 4-inch element (coarse). The resulting deformations were quite similar in shape, and the general type of failure was localized breaching in the immediate area of the charge, with shear failure along the floor and side wall. Figure 10 shows the deformed shapes for the original and current versions. The original model's sudden stress release upon uniaxial tensile fracture explains the backface spalling and large boundary deformations. The original model excessive energy dissipation in biaxial tension explains the

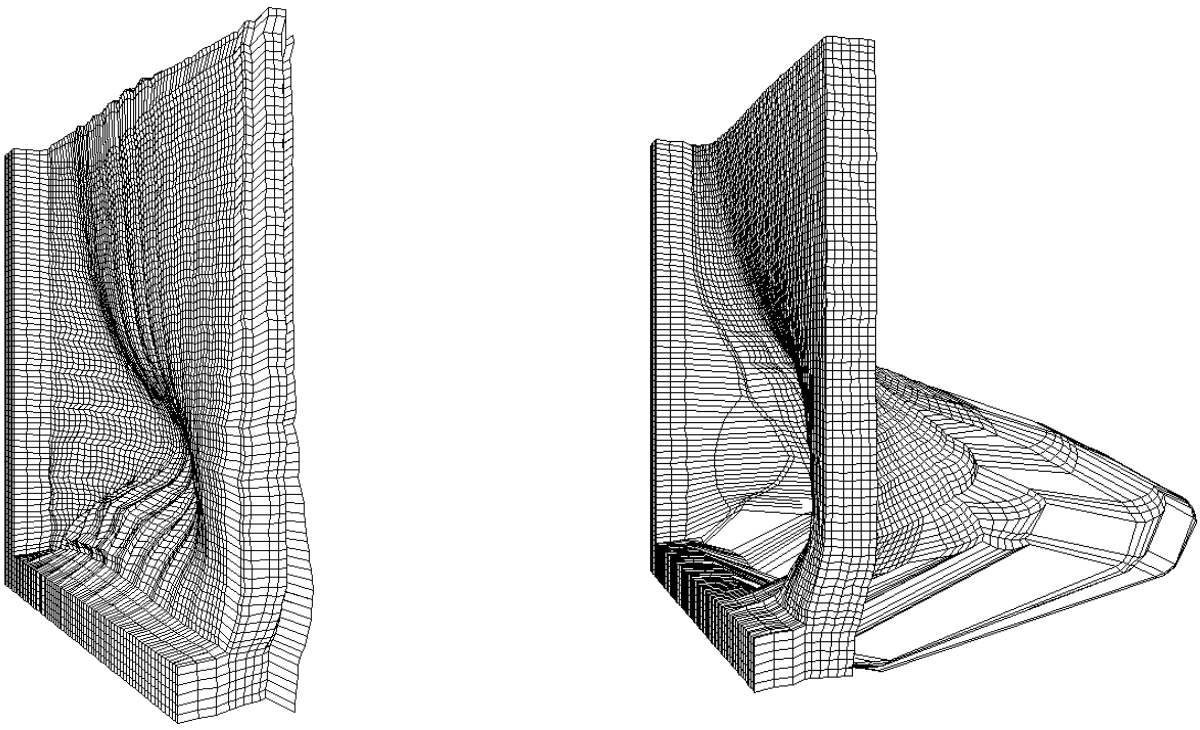

(a) Original version. (b) Current version

Figure 10. Comparative results for original and current versions.

reduced deformations at the load level.

Figure 11 shows the horizontal velocity of a node on the front face of the slab located approximately one foot above the intersection of the dividing wall with the floor, in line with the charge. This represents the location of maximum velocity and greatest damage. The time histories indicate that the slab has clearly failed since there is little or no late time reduction in velocity due to failure of the concrete and reinforcing steel. The calculations predicted fragment velocities 470 ft/s for the fine mesh. This compares well with the expected 500 ft/s and is a clear improvement on the 170 ft/s prediction with the original model.

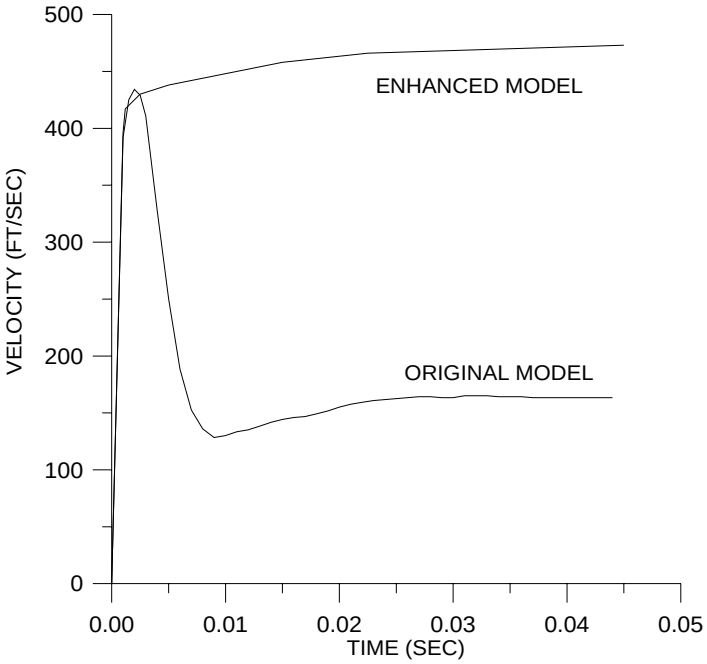

Figure 11. Velocity time histories.

In conclusion, the tests results appear to confirm the validity of the analytical models, both with regard to the predicted secondary fragment velocity as well as the level and mode of damage incurred by the dividing walls. Significant improvements were obtained with the enhanced version of the concrete material model.

IMPLEMENTATION OF SHEAR DILATION

EXPERIMENTAL OBSERVATIONS

Concrete subjected to shear stresses exhibits dilation in the direction transverse to the shear stress plane. Upon cracking the dilation is expected to continue due to aggregate interlock until the crack opening is large enough to clear the aggregates on both sides. This implies there is a limit in the amount of dilatancy.

In the presence of a constraint normal to the shearing plane, such as an external force or steel reinforcement across the plane, the shear capacity across the plane increases. This can be observed in tests by K&C [14] (Figure 12) and Reinhardt and Walraven [15] (Figure 13) among others [16]. In the tests by K&C the joint was tested both monolithically (uncracked) and precracked.

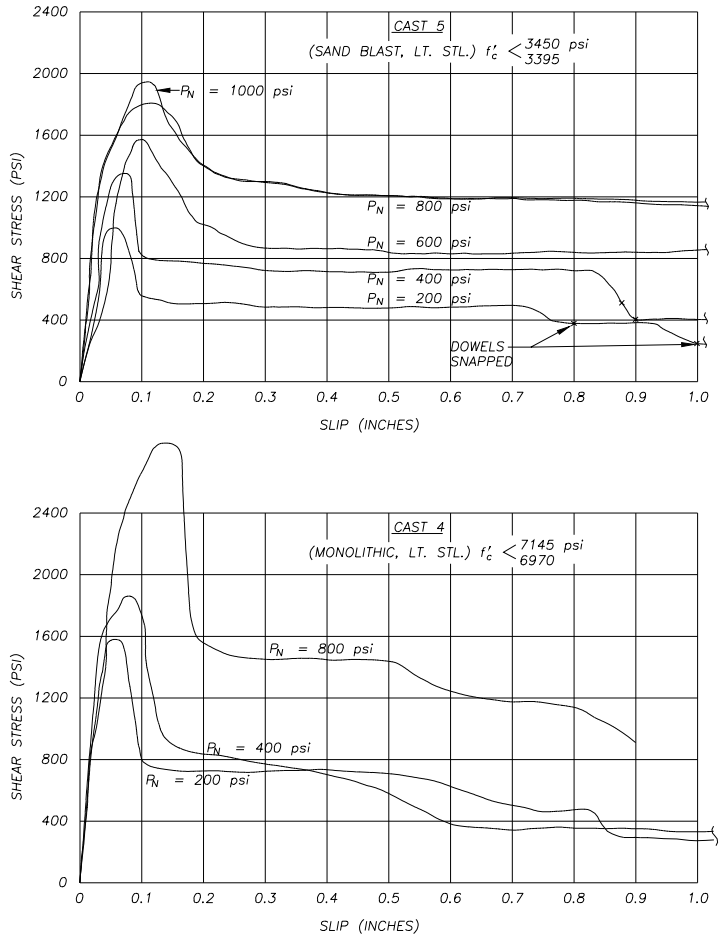

Figure 12. Effect of lateral pressure on shear transfer across a joint, from [14].

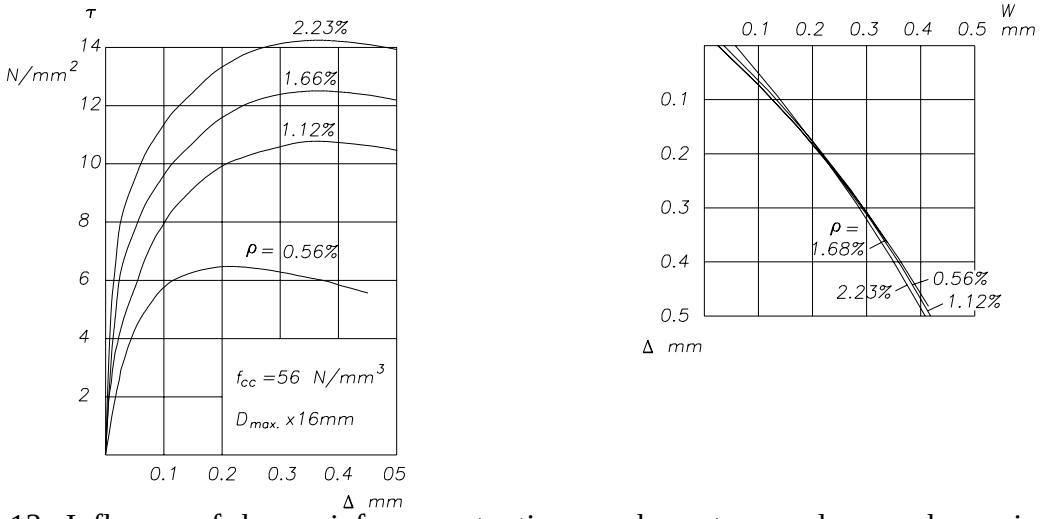

Figure 13. Influence of shear reinforcement ratio ρ on shear stress and on crack opening [15].

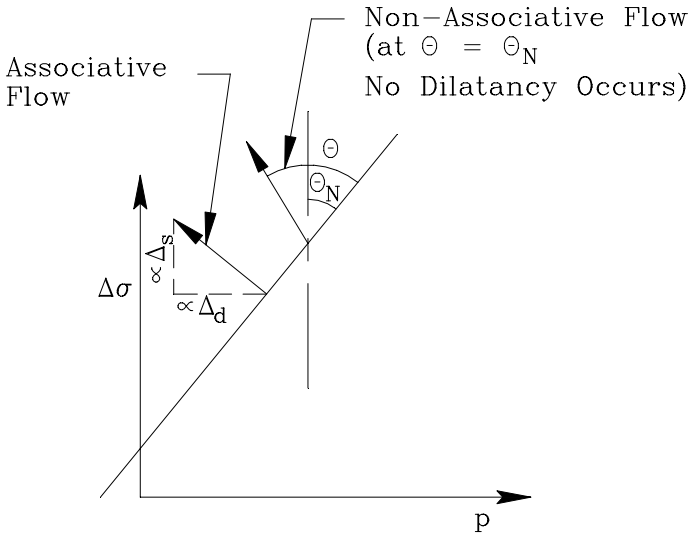

Figure 14. Associative and non-associative flow rule.

THEORY AND IMPLEMENTATION

In the original version, a constant volume Prandtl-Reuss model had been implemented. This is a particular case of non-associative flow rule ($\theta=\theta_N$ in Figure 14). That model has the shortcoming of not being able to represent the dilatancy due to shearing. Other models have implemented associative flow, where the plastic strain increment is normal to the failure surface (Figure 14). However it is known that this yields excessive dilation due to shear. In the current version a general non-associative flow rule is implemented [17,18] where the amount of partial associativity is indicated by an input parameter ω.

PRANDTL-REUSS (NON-DILATANT) FLOW RULE

To set the stage for the partially associated flow rule, the non-dilatant one is first derived. In matrix symbolic notation, the decomposition of strain increments into elastic and plastic parts is

$$d\varepsilon = d\varepsilon^p + d\varepsilon^e = \sigma' d\mu + C d\sigma$$

where σ' is the deviatoric stress and C the (fourth order) elastic tensor, and where we have assumed Prandtl-Reuss (volume-preserving) plastic flow. Premultiplying by C^{-1},

$$C^{-1}d\varepsilon = C^{-1}\sigma' d\mu + d\sigma \quad . \qquad (1)$$

The left-hand side of (1) is the "trial elastic stress increment" $d\sigma^*$, and $C^{-1}\sigma' = 2G\sigma'$, where G is the shear modulus, so (1) simplifies to

$$d\sigma^* = 2G\sigma' d\mu + d\sigma \quad . \qquad (2)$$

(In this discussion we regard the pressure change as part of the trial elastic increment, since with Prandtl-Reuss flow it can be computed immediately and completely once the strain is known.) Multiplying (2) by $\nabla_\sigma f$, the gradient with respect to stress of the failure function $f = \sqrt{3J_2'} - Y(\sigma,\lambda)$,

$$(\nabla_\sigma f)\, d\sigma^* = 2G(\nabla_\sigma f)\, \sigma' d\mu + (\nabla_\sigma f)\, d\sigma \quad . \quad (3)$$

Here, Y is proportional to the radius of the failure surface measured normal to the hydrostatic axis in principal stress space, and λ is the hardening parameter. Now by differentiating the consistency equation $f(\sigma, \lambda) = 0$ (which ensures that the stress point remains on the failure surface during plastic flow), we have

$$(\nabla_\sigma f)\, d\sigma + f_{,\lambda} d\lambda = 0 \;\Rightarrow\; (\nabla_\sigma f)\, d\sigma = -f_{,\lambda} d\lambda = Y_{,\lambda} d\lambda \qquad (4)$$

where the comma denotes a partial derivative. Using (4) in (3) gives

$$(\nabla_\sigma f)\, d\sigma^* = 2G(\nabla_\sigma f)\, \sigma' d\mu + Y_{,\lambda} d\lambda \quad . \qquad (5)$$

On the other hand, the increment in the hardening parameter λ will be related to the plastic strain increment:

$$d\lambda = h(\sigma) d\overline{\varepsilon^p} = h(\sigma)\sqrt{(2/3) d\varepsilon_{ij}^p d\varepsilon_{ij}^p} = h(\sigma)\sqrt{(2/3)\sigma':\sigma'}\, d\mu = g(\sigma) d\mu \qquad (6)$$

where we have defined $g(\sigma) = h(\sigma)\sqrt{(2/3)\sigma':\sigma'}$. In this model we further define

$$h(\sigma) = \begin{cases} [1 + (s/100)(r_f - 1)]^{-1}\left(1 + p / r_f \mathrm{f_t}\right)^{-b_1} & , \quad p > 0 \quad , \\ [1 + (s/100)(r_f - 1)]^{-1}\left(1 + p / r_f \mathrm{f_t}\right)^{-b_2} & , \quad p < 0 \quad , \end{cases}$$

where the parameters are defined in Section 4.2. By substituting $d\lambda$ from (6) into (5) and solving for $d\mu$,

$$d\mu = \frac{(\nabla_\sigma f) d\sigma^*}{2G(\nabla_\sigma f)\sigma' + Y_{,\lambda} g(\sigma)} \quad . \qquad (7)$$

Equation (7) can be made more explicit by rewriting the failure function in terms of stress invariants. The case of interest has

$$f(\sigma, \lambda) = \sqrt{3J_2'} - \hat{Y}(p, \theta, \lambda) \qquad (8)$$

where θ is the Lode angle, which satisfies

$$\cos(3\theta) = \frac{3\sqrt{3} J_3'}{2(J_2')^{3/2}} \quad .$$

By the chain rule, the components of the gradient with respect to stress of (8) can be written

$$\frac{\partial f}{\partial \sigma_{ij}} = \frac{3}{2\sqrt{3J_2'}} \frac{\partial J_2'}{\partial \sigma_{ij}} - \frac{\partial \hat{Y}}{\partial p} \frac{\partial p}{\partial \sigma_{ij}} - \frac{\partial \hat{Y}}{\partial (\cos 3\theta)} \frac{\partial (\cos 3\theta)}{\partial \sigma_{ij}} \quad . \qquad (9)$$

The required derivatives are

$$\begin{aligned} \frac{\partial p}{\partial \sigma_{ij}} &= \frac{\partial(-\sigma_{mm}/3)}{\partial \sigma_{ij}} = -\frac{\delta_{ij}}{3} \quad , \\ \frac{\partial (\cos 3\theta)}{\partial \sigma_{ij}} &= \frac{\partial (\cos 3\theta)}{\partial J_2'} \frac{\partial J_2'}{\partial \sigma_{ij}} + \frac{\partial (\cos 3\theta)}{\partial J_3'} \frac{\partial J_3'}{\partial \sigma_{ij}} \quad , \\ \frac{\partial J_2'}{\partial \sigma_{ij}} &= \frac{\partial(\sigma'_{mn}\sigma'_{mn}/2)}{\partial \sigma_{ij}} = \ldots = \sigma'_{ij} \quad , \\ \frac{\partial J_3'}{\partial \sigma_{ij}} &= \frac{\partial(\sigma'_{kl}\sigma'_{lm}\sigma'_{mn}/3)}{\partial \sigma_{ij}} = \ldots = \sigma'_{im}\sigma'_{jm} - \sigma'_{nm}\sigma'_{nm}\frac{\delta_{ij}}{3} \quad . \end{aligned} \qquad (10)$$

Now (9) and (10) can be used to write the first term of the denominator of (7) in the form

$$2G \frac{\partial f}{\partial \sigma_{ij}} \sigma'_{ij} = 2G\sqrt{3J_2'} \quad . \qquad (11)$$

It is very interesting to note that the gradient terms involving the Lode angle and pressure derivatives vanish. There is a geometrical explanation for this: In principal stress space, (11) is a dot product between two vectors, the gradient and the deviatoric stress. At the current stress

point, decompose the gradient into three orthogonal components, in the directions of p, σ', and θ. Only the component in the direction of σ', corresponding to the first term on the r.h.s. of (9), contributes to the dot product.

Using (11) in (7),

$$d\mu = \frac{(\nabla_\sigma f)\, d\sigma^*}{2G\sqrt{3J_2'} + \hat{Y}_{,\lambda} g(\sigma)} \quad . \quad (12)$$

From an analytical standpoint, equation (12) completes the incremental solution to the problem, since it could be used in (2) and (6) to give $d\sigma$ and $d\lambda$ in terms of $d\varepsilon$.

RADIAL RETURN IN THE NUMERICAL IMPLEMENTATION

In preparation for numerical implementation, (12) can be simplified somewhat by observing that if σ_n is the stress at the beginning of the current time step, then $f(\sigma_n) = 0$, so a Taylor series expansion gives $f(\sigma^*) = f(\sigma_n + d\sigma^*) \cong (\nabla_\sigma f) d\sigma^*$. But by definition, $f(\sigma^*) = \sqrt{3J_2'^*} - Y^*$. Thus

$$d\mu = \frac{\sqrt{3J_2'^*} - Y^*}{2G\sqrt{3J_2'} + Y_{,\lambda} g(\sigma)} \quad . \quad (13)$$

For an accurate, efficient numerical solution, more work is required, in part because using just the first-order equations (2,6,12) would not leave the stress point precisely on the failure surface at the end of the time step. Therefore the idea of "radial return" is introduced. Equation (2) shows that the stress increment $d\sigma$ can be regarded as consisting of two parts: the elastic trial increment and a second part which is collinear with the current deviatoric stress itself. In principal stress space, any "stress vector" parallel to a purely deviatoric one is normal to the hydrostatic axis. Since at the end of the time step the stress point must be on the failure surface, the second part of the stress increment can be considered a "radial return" to the failure surface in a plane normal to the hydrostat. The difficulty is to know where the failure surface should be at the end of the time step, because it will have moved during the time step. Our function $\hat{Y}$ depends on pressure and Lode angle as well as hardening parameter. However, neither of the first two changes during the radial return, so their effect on $\hat{Y}$ will be fully accounted for by the elastic trial stress increment, and it is only necessary to consider the hardening parameter's effect on the failure surface location once the trial elastic increment is applied. The procedure is therefore to locate the failure surface according to the trial elastic stresses, then to use essentially a first order approximation for the increment in the hardening parameter to further move the failure surface due to strain hardening, and finally to radially scale the deviatoric stress components back from the trial elastic point so that they lie exactly on the new surface. In fact the only reason for computing $d\mu$ is to use it in the first order approximation for the new failure surface location. The stress changes during the last step would of course agree to first order with those corresponding to the negative of the first term on the right-hand side of (2), but the radial return scheme guarantees that the stress point will be on the failure surface, to within machine accuracy, at the end of each finite time step.

Now recall that Y^* denotes the failure surface corresponding to the updated pressure and deviatoric stresses including the trial elastic stress increment, but the *prior* value of λ. If Y_{n+1} denotes the *fully* updated surface, the increment due to λ alone is approximated as

$$Y_{n+1} - Y^* = \hat{Y}_{,\lambda} d\lambda = \hat{Y}_{,\lambda} g(\sigma^*) d\mu = \frac{\hat{Y}_{,\lambda} g(\sigma^*)(\sqrt{3J_2'^*} - Y^*)}{2G\sqrt{3J_2'^*} + \hat{Y}_{,\lambda} g(\sigma^*)} \quad . \qquad (14)$$

This is the update to the failure surface after the trial elastic part. It only remains to scale back the trial stress by the factor that follows from (14):

$$\sigma_{n+1} = \left[1 + \frac{\hat{Y}_{,\lambda} g(\sigma^*)}{2G\sqrt{3J_2'^*} + \hat{Y}_{,\lambda} g(\sigma^*)} \left(\frac{\sqrt{3J_2'^*}}{Y^*} - 1 \right) \right] \sigma^* \quad . \qquad (15)$$

FRACTIONALLY ASSOCIATED FLOW

If the plastic flow were fully associated, we would have

$$d\varepsilon^{p,assoc} = (\nabla_\sigma f) d\tilde{\mu}$$

where $d\tilde{\mu}$ is a proportionality constant. Again, consider the components of the gradient in principal stress space, in the directions of p, σ', and θ. Assume the θ-component does not produce plastic flow, and that the p-component produces only a fraction ω of that which would occur if fully associated. With reference to (8,9,10), the plastic strain components are then

$$d\varepsilon_{ij}^{p,\omega} = \left(\frac{3}{2\sqrt{3J_2'}} \frac{\partial J_2'}{\partial \sigma_{ij}} - \omega \frac{\partial \hat{Y}}{\partial p} \frac{\partial p}{\partial \sigma_{ij}} \right) d\tilde{\mu} = \left(\frac{3\sigma_{ij}'}{2\sqrt{3J_2'}} + \frac{\omega \hat{Y}_{,p} \delta_{ij}}{3} \right) d\tilde{\mu} = (\sigma_{ij}' + m\delta_{ij}) d\mu$$

or, symbolically,

$$d\varepsilon^p = (\sigma' + mI) d\mu \ , \ (16)$$

where $m = 2\omega\sqrt{3J_2'}\hat{Y}_{,p} / 9$, I is the identity tensor, and where the proportionality constant $d\mu$ is just a re-scaled version of $d\tilde{\mu}$. Proceeding analogously with the non-dilatant case, the full strain increment is

$$d\varepsilon = (\sigma' + mI) d\mu + C d\sigma \quad . \quad (17)$$

Noting that $C^{-1} I = 3KI$ where K is the bulk modulus, (17) becomes

$$d\sigma^* = (2G\sigma' + 3mKI) d\mu + d\sigma \quad . \qquad (18)$$

Multiplying by the stress gradient, using (4) and (6), and solving for $d\mu$,

$$d\mu = \frac{(\nabla_\sigma f) d\sigma^*}{2G(\nabla_\sigma f)\sigma' + 3mK(\nabla_\sigma f) I + \hat{Y}_{,\lambda} g(\sigma)} \quad . (19)$$

Noting that

$$(\nabla_\sigma f) I = \frac{\partial f}{\partial \sigma_{kk}} = -\hat{Y}_{,p} \frac{\partial p}{\partial \sigma_{kk}} = \hat{Y}_{,p} \quad ,$$

and using (11), the definition of m following (16), and the comments preceding (13), equation (19) simplifies to

$$d\mu = \frac{\sqrt{3J_2'^*} - Y^*}{2G\sqrt{3J_2'}\left(1 + \dfrac{\omega K \hat{Y}_{,p}^2}{3G}\right) + \hat{Y}_{,\lambda} g(\sigma)} \quad . \qquad (20)$$

Now assume the radius of the failure surface takes the form

$$\hat{Y}(p,\theta,\lambda) = \hat{r}[\psi(p),\theta]\hat{Y}_c(p,\lambda) \quad ,$$

where $\hat{Y}_c(p,\lambda)$ is the compressive meridian (i.e., the failure surface in conventional triaxial compression, at θ=60°), $\psi(p)$ is the ratio of the failure surface radius in extension to compression, and $\hat{r}[\psi(p),\theta]$ is a dimensionless function giving the current radius of the failure surface as a fraction of the compressive meridian. In the current K&C/LRDA version of DYNA3D model 16, $\psi(p)$ varies from 1/2 to unity as pressure varies from the minimum allowable (set to the negative of the tensile strength) to positive infinity; while the function $\hat{r}(\psi,\theta)$ is based on the Willam-Warnke failure surface and takes the form

$$\hat{r}(\psi,\theta) = \frac{2(1-\psi^2)\cos\theta + (2\psi-1)\sqrt{4(1-\psi^2)\cos^2\theta + 5\psi^2 - 4\psi}}{4(1-\psi^2)\cos^2\theta + (1-2\psi)^2} \quad .$$

One effect of this formulation is to complicate the algebra needed to compute $d\mu$ (and subsequently – through equation (16) – the plastic volumetric strain increment). The p-derivative in (19) will involve not only the variation of the compressive meridian $\hat{Y}_c(p,\lambda)$, but also the variation of $\hat{r}[\psi(p),\theta]$.

IMPLEMENTATION OF FRACTIONAL ASSOCIATIVITY

Here, in order, is an outline of the numerical procedure for updating the stresses. On entering the subroutine (f3dm16), the total strains will already have been updated according to the equation of motion. Three successive stress states are involved: *current*, denoted with the subscript n , where the stresses are those from the previous time step; *trial elastic*, denoted by superscript * , where the stresses have been updated according to certain elastic moduli and strain increments to be detailed below; and *final*, denoted by subscript *n+1*, the fully updated state.

1. Compute the bulk modulus K and trial elastic pressure p* from the EOS based on the difference between the total volume strain and the current plastic volume strain. The latter must be stored and updated for each element throughout the course of the calculation. The array epx5 is used for this purpose. It had been used for the tensile cutoff in the original model 16, but is no longer needed for that purpose since now the tensile cutoff is incorporated in the failure surface. The structure of DYNA3D requires that the strain difference be computed in subroutine sueos8, called from within f3dm16, so a minor change to the former is required.

2. Compute the shear modulus based on bulk modulus, Poisson's ratio, and the extent of unloading in the pressure-vs-elastic volume relationship

3. Compute the trial elastic deviatoric stress increments based on the shear modulus and total deviatoric strain increments. Add them to the current deviatoric stresses and combine with the trial elastic pressure to give the full trial stress state σ^*.

4. Compute the Lode angle corresponding to the trial elastic state. Since flow is nonassociated in deviatoric planes, this angle will not change any further. It becomes θ_{n+1}

5. Compute Von Mises effective stress $\sqrt{3J_2'^*}$ and failure surface radius $Y^* = \hat{\hat{Y}}(p^*, \theta_{n+1}, \lambda_n)$, the latter based on the trial elastic pressure, trial elastic Lode angle, and current damage parameter λ_n. If $\sqrt{3J_2'^*} < Y^*$, this increment is elastic, the trial state becomes the final state, and no further computation is required.

6. Compute $d\mu$ from (20), basing all stress-dependent terms on the trial elastic stresses. As noted in the discussion following (20), the pressure derivative $\hat{Y}_{,p}$ is complicated.

7. The final failure surface Y_{n+1} will differ from Y^* due both to a further change in pressure (from the trial elastic state) and to the increment $d\lambda$ in the damage parameter. Therefore, compute a final failure surface radius from
$$Y_{n+1} = Y^* + \hat{Y}_{,p}\, dp^p + \hat{Y}_{,\lambda} d\lambda$$
The increments in this formula are computed as follows: from (18) the additional pressure increment dp^p is $3mKd\mu$. From (6), using the trial elastic stress we have $d\lambda = g(\sigma^*)d\mu$.

8. Scale the deviatoric stress components back to the final failure surface according to
$$\sigma'_{n+1} = (Y_{n+1} / Y^*)\sigma'^*$$
9. Update the pressure, damage parameter, and plastic volumetric strain according to
$$p_{n+1} = p^* + dp^p\ ,\ \lambda_{n+1} = \lambda_n + d\lambda\ ,\ \varepsilon^{pv}_{n+1} = \varepsilon^{pv}_n + 3md\mu$$
the latter following from (16).

APPLICATION TO LATERALLY CONFINED CONCRETE CYLINDERS

Lateral confinement of circular columns via steel or composite jackets significantly enhances the columns ductility when subjected to strong motion earthquakes and blast loads. The column jacketing system is dependent on the lateral dilation of the concrete for development of the confining action. Concrete in uniaxial unconfined compression exhibits a constant Poisson ratio of about 0.2 until approximately 75% of the compressive strength, corresponding to a volumetric compression phase. At that point extensive internal cracking starts developing and the apparent Poisson ratio starts increasing to 0.5, where there is no further volume variation. For increasing compression the apparent Poisson ratio keeps increasing until the overall volumetric strain becomes zero, then becomes positive (net volume increase). This is shown in qualitatively in Figure 15a [19]. The ability of the numerical material model to reproduce the volumetric expansion phase is the key to the proper representation of the jacketing confinement

effect. Figure 15b shows the corresponding output from the new concrete material model for a single concrete element.

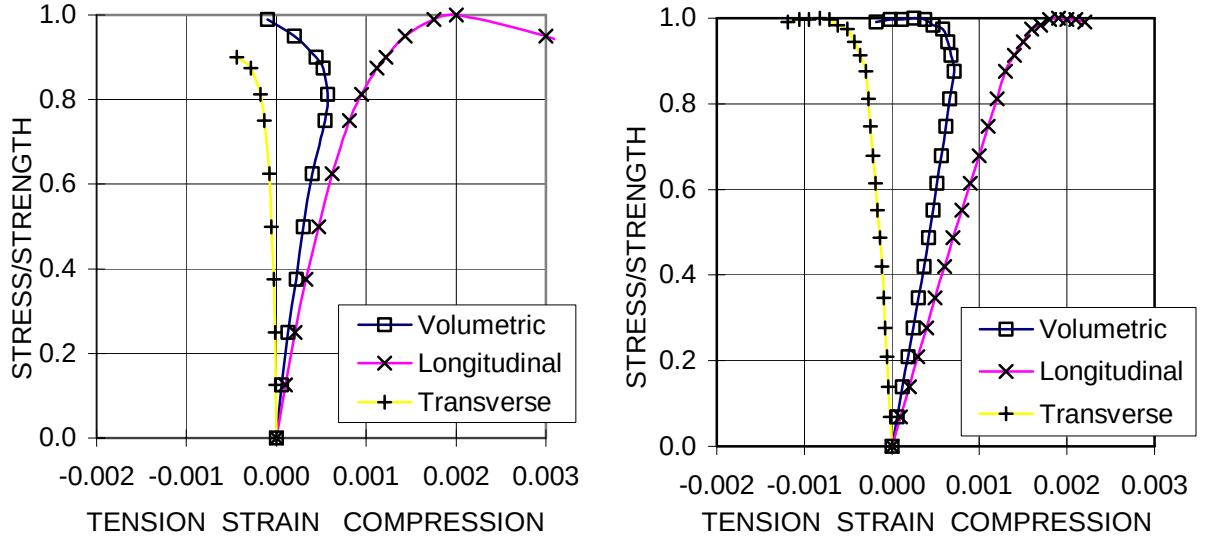

(a) Typical test results (b) numerical model predictions

Figure 15. Strain histories in an uniaxial unconfined compression test.

ASTM C39 compression tests carried out on 6-inch (15.2 cm) diameter concrete cylinders jacketed with two layers of a carbon composite resulted in a strength increase of 20% at a peak strain of about 0.005. Figure 16a shows the test results for plain and jacketed concrete cylinders. Figure 16b shows the DYNA3D predictions for both cases. It is apparent that the material model is able to properly represent the jacketing effects.

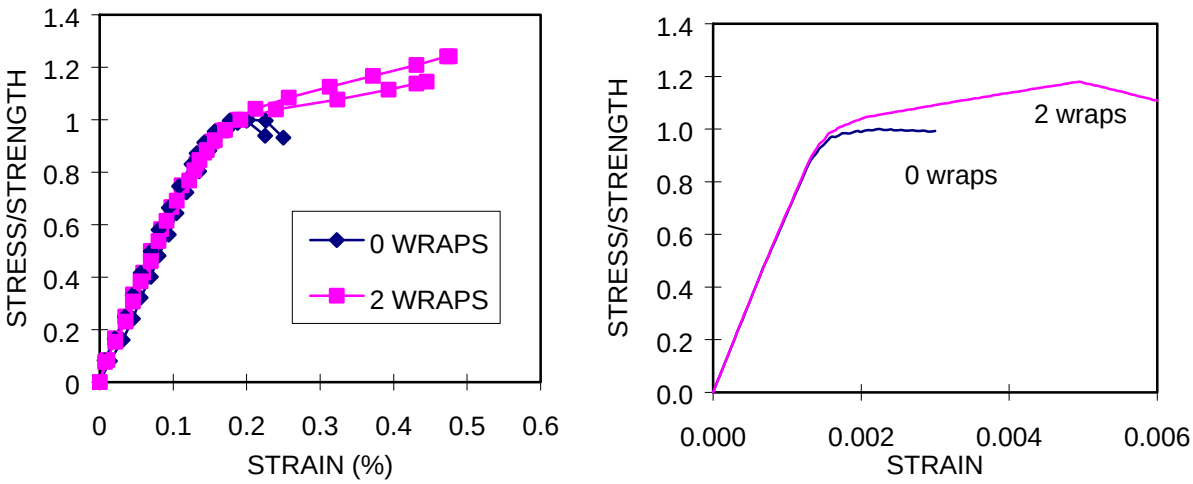

(a) Test results (b) Numerical model

Figure 16. Compression test results on standard cylinders with and without wraps.

CONCLUSIONS

The concrete material model in DYNA3D was significantly modified to properly represent material behavior along multiple radial paths in the $\Delta\sigma$ versus p space, including uniaxial, biaxial and triaxial tension and compression. The plasticity model was extended to replace the tensile cutoff and provide a smooth transition to the residual failure surface. A new algorithm captured strain rate effects properly in any radial path. This enhanced Prandtl-Reuss model has shown to properly represent the blast response of Substantial Dividing Walls subjected to standard charges.

Further modifications were implemented to include shear dilation. This latter model was then applied to the case of laterally restrained cylinders under uniaxial compression.

REFERENCES

1. Whirley, R.G, Hallquist, J.O., *DYNA3D: A Nonlinear Explicit Three-Dimensional Finite Element Code for Solid and Structural Mechanics, User Manual*, Report UCRL-MA-107254, Lawrence Livermore National Laboratory, Livermore, CA, May 1991.
2. Malvar, L.J., Crawford, J.E., Wesevich, J.W., Simons, D., *A New Concrete Material Model for DYNA3D*, Report No. TM-94-14 to the Defense Nuclear Agency, Karagozian & Case, Glendale, CA, December 1994.
3. Malvar, L.J., Crawford, J., Simons, D., Wesevich, J.W., "A New Concrete Material Model for DYNA3D," *Proceedings, 10th ASCE Engineering Mechanics Conference*, vol. 1, Boulder, CO, May 1995, pp. 142-146.
4. Shugar, T.A., Holland, T.J., Malvar, L.J., "Applications of Finite Element Technology to Reinforced Concrete Explosive Containment Structures," *Proceedings, Twenty-Fifth DOD Explosive Safety Seminar*, Anaheim, CA, August 1992.
5. Malvar, L.J., Crawford, J.E., Wesevich, J.W., Dunn, B., *Modifications to DYNA3D Material Model 16*, Report No. TM-93-13 to the Defense Nuclear Agency, Appendix B, Karagozian & Case, Glendale, CA, June 1993.
6. Comite Europeen du Beton - Federation Internationale de la Precontrainte, *CEB-FIP Model Code 90*, 1990
7. Chen, W.F., *Plasticity in Reinforced Concrete*, McGraw-Hill Book Co., New York, 1982.
8. Kupfer, H., Hilsdorf, H., Rush, H., "Behavior of Concrete under Biaxial Stresses," *ACI Journal*, Vol. 66, pp. 656-666, 1969.
9. Ahmad, S.H., Shah, S.P., "Complete Triaxial Stress-Strain Curves for Concrete," *Journal of the Structural Division, ASCE*, Vol. 108, No. ST4, April 1982, pp. 728-742.
10. Bogosian, D., *Parametric Analysis of 12-Inch Substantial Dividing Walls*, Report No. TM-94-20, Karagozian and Case, CA, 1994.
11. *SHOCK User's Manual*, Version 1.0, Naval Civil Engineering Laboratory, Port Hueneme, CA, January 1988.
12. *FRANG User's Manual*, Naval Civil Engineering Laboratory, Port Hueneme, CA, May 1989.

13. Schwartz, A., *Report on Summary and Analysis of Full Scale Dividing Wall Tests and Comparisons with Analytically Predicted Results*, Picatinny Arsenal, Dover, NJ, March 1964.
14. K&C Structural Engineers, *Construction Joint Test Program*, Final Report Contract No. F04701-72-C-0358, Karagozian & Case, Glendale, CA, 1973.
15. Reinhardt, H.W., and J.C. Walraven, "Cracks in Concrete Subject to Shear," *Journal of the Structural Division*, Vol. 108, No. ST1, January 1982, pp. 207-224.
16. Malvar, L.J., "Mixed Mode Fracture in Concrete," *Proceedings, First Intl. Conference on Fracture Mechanics of Concrete Structures*, Breckenridge, CO, pp. 677-688, June 1992.
17. Simons, D., "Recent Modifications to DYNA3D Model 16 for Concrete," *Proceedings, DNA CWE Structural Analysis Meeting*, Logicon RDA, Albuquerque, NM, Jan 1995, pp. 141-157.
18. Malvar, L.J., Crawford, J.E., Wesevich, J.W., Simons, D., *A New Concrete Material Model for DYNA3D, Release II: Shear Dilation and Directional Rate Enhancements*, Report No. TM-96-2 to the Defense Nuclear Agency, Karagozian & Case, Glendale, CA, Dec 1994.
19. Park, R., Paulay, T., *Reinforced Concrete Structures*, John Wiley & Sons, NY, 1975, 769 pp.